Novel UV–Visible Photodetector in Photovoltaic Mode with Fast Response and Ultrahigh Photosensitivity Employing Se/TiO_2 Nanotubes Heterojunction

*Lingxia Zheng, Kai Hu, Feng Teng, and Xiaosheng Fang**

***A** feasible strategy for hybrid photodetector by integrating an array of self-ordered TiO_2 nanotubes (NTs) and selenium is demonstrated to break the compromise between the responsivity and response speed. Novel heterojunction between the TiO_2 NTs and Se in combination with the surface trap states at TiO_2 help regulate the electron transport and facilitate the separation of photogenerated electron–hole pairs under photovoltaic mode (at zero bias), leading to a high responsivity of ≈100 mA W^{-1} at 620 nm light illumination and the ultrashort rise/decay time (1.4/7.8 ms). The implanting of intrinsic p-type Se into TiO_2 NTs broadens the detection range to UV–visible (280–700 nm) with a large detectivity of over 10^{12} Jones and a high linear dynamic range of over 80 dB. In addition, a maximum photocurrent of ≈10^7 A is achieved at 450 nm light illumination and an ultrahigh photosensitivity (on/off ratio up to 10^4) under zero bias upon UV and visible light illumination is readily achieved. The concept of employing novel heterojunction geometry holds great potential to pave a new way to realize high performance and energy-efficient optoelectronic devices for practical applications.*

1. Introduction

1D semiconductor nanostructures have stimulated much attention in high performance photodetectors (PDs) owing to the pronounced surface effects (i.e., oxygen adsorption/desorption) originating from the large surface-to-volume ratio and a Debye length comparable to their small size for 1D semiconductor nanostructures.[1–5] Generally, the large surface-to-volume ratio can significantly increase the number of surface trap states and prolong the photocarrier lifetime, leading to good sensitivity and high responsivity.[1] However, the surface effects also extend the rise/decay time due to slow oxygen adsorption/desorption processes, thus hindering the practical applications of 1D semiconductor nanostructures in PDs.[4] Several strategies to solve this compromise for enhancing the responsivity as well as the response time have been developed, including the introduction of Schottky junction and heterojunction,[6–8] modification of surfaces,[9,10] optimization of nanowire/nanotube sizes,[11,12] and the fabrication of network geometries.[13]

Heterojunction nanocomposites between different materials have shown great potential for the applications in solar cells, biosensors, photodetectors, and piezoelectric nanogenerators[4,14–17] due to their multifunctionality. In addition, junctions are essential for photovoltaic device to create built-in electric field, which acts like a driving force to efficiently separate photogenerated electron–hole pairs. By implanting heterojunction in PDs, self-powered devices can detect at zero volt bias using internal photovoltaic effect and without consuming external power. This interesting feature will make devices more reliable and will meet the demands of energy-saving and low-carbon age. To date, self-powered PDs are urgently needed in a large variety of optoelectronics applications including imaging, light-wave communications,

Dr. L. X. Zheng, K. Hu, Dr. F. Teng, Prof. X. S. Fang
Department of Materials Science
Fudan University
Shanghai 200433, P. R. China
E-mail: xshfang@fudan.edu.cn

DOI: 10.1002/smll.201602448

the wire-free route for artificial vision, etc.[18–21] In the field of light-wave optical systems, self-powered wireless PDs are extensively used in optical receivers and fiber optic communication.[20] Without the need of external driving forces, self-powered PDs can achieve a very low dark current and a small photocurrent response due to the weak electric field compared with those devices working under a large external bias. Hence, one of the challenges for self-powered PDs is to increase photocurrent response, thereby enhancing the photosensitivity (on/off ratio).

Among wide bandgap semiconductor candidates, 1D titania nanotube (TiO_2 NT) arrays fabricated by a powerful and efficient electrochemical approach (anodization) have aroused considerable interest in the opto/electronic devices owing to their ease of fabrication, large device area, low cost,[22–24] and superior performances, e.g., excellent light-trapping, large specific surface area, well-defined charge carriers transport pathway and so on.[11,25–27] Nevertheless, the rapid recombination of photogenerated electron–hole pairs leads to a low quantum efficiency and poor photodetection performance. In this study, dramatically enhanced photodetector performances are readily achieved by simply introducing selenium into 1D TiO_2 NTs via a novel heterojunction geometry. As an important semiconductor, selenium (Se) has been reported to exhibit many unique properties, such as high conductivity (≈0.8^5 S cm^{-1}), a relatively low melting point (≈490 K), and high piezoelectric, thermoelectric and nonlinear optical responses.[28–31] The exploring of Se/TiO_2 heterojunction PD demonstrates an ultrasensitive (on/off ratio up to 10^4), superfast (rise/decay time of 1.4/7.8 ms), and broad-band (UV–visible) photodetection without external energy supply. With the aid of p–n junction, the photogenerated carriers are efficiently separated by the built-in electric field. Accordingly, a large detectivity of over 10^{12} Jones and a maximum linear dynamic range of ≈100 dB are obtained at zero bias. The high responsivity of ≈100 mA W^{-1} at 620 nm light illumination, fast respond speed as well as the ultrahigh on/off ratio are comparable to those best-reported values for other self-powered PDs (**Table 1**). The excellent broadband photodetection results reveal that the Se/TiO_2 p–n junction geometry holds great potential in realizing future large-scale, high performance, and energy-efficient PDs.

2. Results and Discussion

The structural morphologies of the TiO_2-based samples are revealed by a field emission scanning electron microscopy (FE-SEM). By employing a two-step anodization approach, a porous thin layer of TiO_2 film is formed on top of the conventional self-ordered nanotubular array with an average inner-tube diameter of ≈65 nm as shown in **Figure 1**a. The porous network with larger pore sizes of 140–200 nm can prevent tube-bundling and allow a high tube-packing density beneficial for specific surface area. It is worthy noticing that the second-anodization process ensures the top-porous network with a clean top surface in providing an easy access for uniform selenium loading, as a large amount of highly disordered and undesirable tube-top structures existed when using one-step anodization process, which is mainly originating from the chemical etching upon exposure to fluoride-containing electrolyte (Figure S1a,b, Supporting Information). The lateral-view SEM image in Figure 1b shows that the overall film thickness is ≈8.5 µm and the average outer-tube diameters are estimated to be ≈160 nm. Typical SEM images of the Se/TiO_2 composite are presented in Figure 1c,d. The uniformly loading of Se is preferentially distributed at the top large pores instead of the self-ordered TiO_2 tubular arrays. From a tilted-view SEM image in Figure 1d, only the thin-layer top-porous film (≈25 nm thick, Figure S1c, Supporting Information) is filled with very small amount of Se while the underneath TiO_2 NTs backbone remains unchanged. The pure Se sample in the absence of TiO_2 NTs was prepared on a silicon substrate with a 200 nm thick SiO_2 top layer for comparison, which shows very dense and thick film morphology (Figure S1d, Supporting Information).

The X-ray diffraction (XRD) patterns of the three as-prepared samples: the anodic TiO_2 NTs, pure Se sample, and Se/TiO_2 composite are displayed in **Figure 2**. The diffraction peaks for the bare TiO_2 NTs appearing at 25.3°, 37.8°, 38.6°,

Table 1. Comparison of the main parameters for Se/TiO_2 heterojunction photodetectors and other self-powered photodetectors in the literature.

PD[a]	Type	Light of detection	On/Off ratio	D*[b] [Jones]	R_λ[c] [A W^{-1}]	τ_r[d] [ms]	τ_d[e] [ms]	Ref.
ZnO/PbS(QDs)/NiO	Double heterojunction	600 nm		1.2×10^{12}		0.0095		[42]
CuO/Si	p–n	405 nm	1×10^3	3×10^9	3.98×10^{-4}	0.06	0.08	[51]
Graphene/MoS_2	Phototransistor	632.8 nm	1428		0.6	0.13	0.13	[57]
PPA/TiN	Hybrid	white light (400–750 nm)	≈70	1.92×10^{11}	0.57	9.23	18.12	[58]
MoS_2/Si	Heterojunction	808 nm		8×10^{13}	0.3	0.003	0.04	[59]
ZnO NRs	MIS	150 W Xe arc lamp		7.99×10^7	1.78×10^{-6}	<100	<100	[60]
Graphene/Si	Schottky	500 nm		5.4×10^{12}	≈0.4	≈6.7	≈8.7	[61]
Se/TiO_2	p–n	620 nm	1.1×10^4	6.2×10^{12}	≈0.1	1.4	7.8	Present work

[a]Photodetector; [b]Detectivity; [c]Responsivity; [d]Rise time; [e]Decay time.

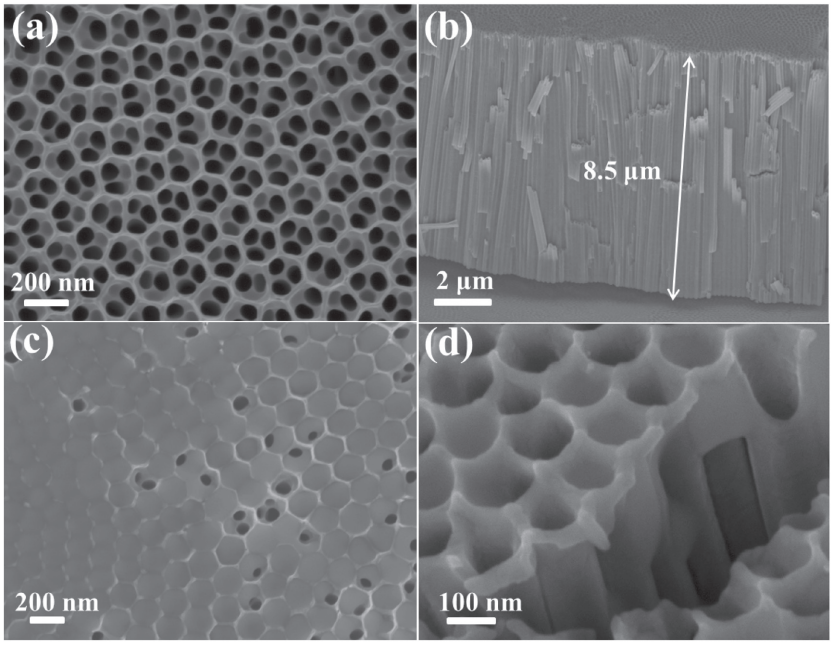

Figure 1. a,c) Plane-view and b,d) tilted-view SEM images of anodic TiO_2 NTs and Se/TiO_2 composite, respectively.

48.1°, 53.9°, and 55.1° are attributed to (101), (004), (112), (200), (105), and (211) crystal planes, respectively, matching well with the standard peaks of anatase TiO_2 (JCPDS No. 21-1272).[32,33] For pure Se sample, all the peak positions and their relative intensities are in good agreement with a hexagonal selenium phase in random crystallographic orientation with lattice parameters of $a = b = 4.364$ Å, $c = 4.959$ Å (JCPDS No. 65-1876), confirming the crystallinity and purity of the as-obtained sample.[34] Obviously, the diffraction patterns for both anatase TiO_2 and hexagonal Se are retained in the composite Se/TiO_2 sample, suggesting the successful introduction of Se into TiO_2 NTs.

The X-ray photoelectron spectroscopy (XPS) analysis was carried out to examine the chemical components and the states of Se/TiO_2 composite as shown in **Figure 3**. The survey spectrum in Figure 3a illustrates that the Se/TiO_2 composite contains dominant elements of Ti, O, Se, and C, where the

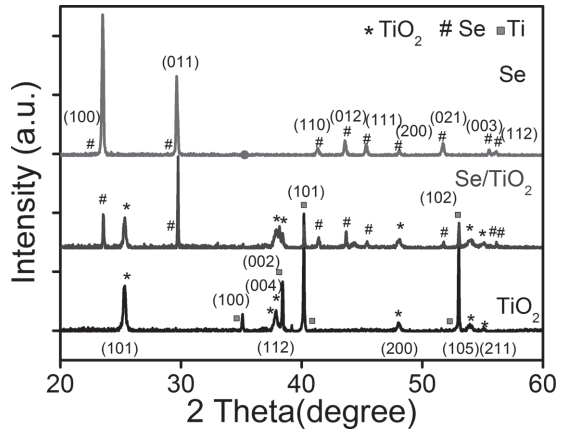

Figure 2. XRD patterns of anodic TiO_2 NTs, pure Se sample, and Se/TiO_2 composite.

peaks of Ti and O are from TiO_2, and the Se peak indicates the presence of Se. As shown in the high resolution Se 3d XPS spectra for pure Se sample and Se/TiO_2 composite in Figure 3b, the binding energy at ≈54.1 eV corresponds to elemental selenium Se(0).[35,36] A comparison of the observed spin-energy separation of ≈5.8 eV between Ti $2p_{1/2}$ and Ti $2p_{3/2}$ peaks indicates a normal chemical state of Ti^{4+} in both pristine TiO_2 NTs and Se/TiO_2 composite (Figure 3c). A lower binding energy of Ti 2p for Se/TiO_2 composite shifted by ≈1 eV is observed, which is possibly due to the successful introduction of Se as the electrons might transfer from Se to TiO_2 .[22]

The photoelectric properties were carefully investigated using a two-probe method at room temperature with respect to Se/TiO_2 composite PD by using silver pads with small area as the electrodes. The device configuration is illustrated in the inset of **Figure 4**a. A typical current–voltage (I–V) curve under dark condition indicates that the device features a rectifying characteristic with a ratio of 24 at ±1 V biases and a turn-on voltage of ≈0.3 V (Figure 4a), indicating a typical photodiode behavior. The I–V curves under UV and visible light illumination were investigated using 350, 450, and 620 nm light. As shown in Figure 4b, a small but measureable photovoltaic effect upon light illumination is readily observed for the three different light wavelengths, indicating that the hybrid device displays an attractive broadband self-powered features (working at zero bias) from UV to visible light. The values for the open-circuit voltage at 620, 450, and 350 nm light illumination are estimated to be 0.20, 0.22, and 0.08 V, respectively. Notably, the photocurrent under both UV and visible light illumination increases obviously at the forward bias, while the device is lowly responsive to visible light (620 and 450 nm) illumination at the reverse bias. The I–V curves for pristine TiO_2 NTs device and pure Se device are shown in Figure 4c,d, respectively. In the dark, the symmetric I–V curves for pristine TiO_2 NTs device indicate that the Schottky junction between the Ag electrodes and TiO_2 is so small and can be negligible, unable to induce self-powered behavior. While the linear I–V curve for pure Se device under dark indicates good ohmic contacts between Ag electrodes and Se (Figure 4d). Thus, the rectification behavior for Se/TiO_2 hybrid device is mainly originating from the heterojunction between Se and TiO_2. Upon light illumination, the pristine TiO_2 NTs device exhibit obvious photoresponse at 350 nm UV light while pure Se device shows broad-band photoresponse upon both UV and visible light illumination (620, 450, and 350 nm), suggesting that selenium plays a dominant role in the photodetection performance for Se/TiO_2 hybrid device. In addition, the electrical transport behavior of bottom-gate Se field-effect transistor (FET) suggests that the Se in this study is an intrinsic p-type semiconductor, as

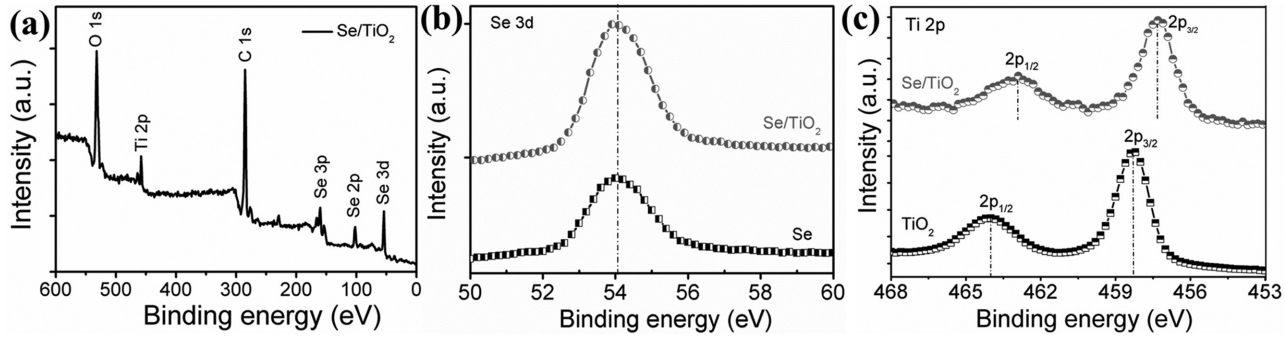

Figure 3. a) XPS survey spectrum of Se/TiO_2 composite. b) The high resolution Se 3d, and c) Ti 2p spectra.

the source-drain current of the FET increases when the gate voltage ($I_{ds} - V_{ds}$) deceases (Figure S2, Supporting Information).[1] Therefore, it is safe to conclude that the small open-circuit voltages in the Se/TiO_2 hybrid device are the main result of p–n junction between Se and 1D TiO_2 NTs, which act as a driving force to separate the photogenerated electron–hole pairs and produce large photocurrent, leading to self-powered response.

The spectral responsivity (R_λ) and external quantum efficiency (EQE) are two important parameters to evaluate the photodetecting performance, which indicates how efficiently a detector responds to optical signals. They can be given by the following equations

$$R_\lambda = \frac{I_{ph} - I_d}{PS} \quad (1)$$

$$\mathrm{EQE} = \frac{hc}{e\lambda} R_\lambda \quad (2)$$

where I_{ph} is the photocurrent, I_d is the dark current, P is the light power density, S is the effective area under irradiation, λ is the exciting wavelength, h is the Planck's constant, c is the velocity of light, and e is the electronic charge. As shown in **Figure 5**a, an obvious high responsivity of the heterostructured Se/TiO_2 device is observed in a wide wavelength range from UV to visible region (280–700 nm). Two dominant peaks are appeared in the visible light range with values of ≈96 mA W^{-1} at 620 nm with EQE of 20% and 55 mA W^{-1} at 450 nm with EQE of 15%. In the UV region (280–390 nm), the R_λ and EQE increase with shorter wavelength. The maximum R_λ is nearly 0.1 A W^{-1} under light illumination of 620 nm at zero bias, comparable to other self-powered PDs (Table 1). For pristine TiO_2 NTs device, the responsivity is observed only in the UV range (280–390 nm) at a bias of 1 V with values increasing with decreasing wavelength (Figure S3a, Supporting Information). While the spectral responsivity profile of pure Se device (Figure S3b, Supporting Information) is very similar

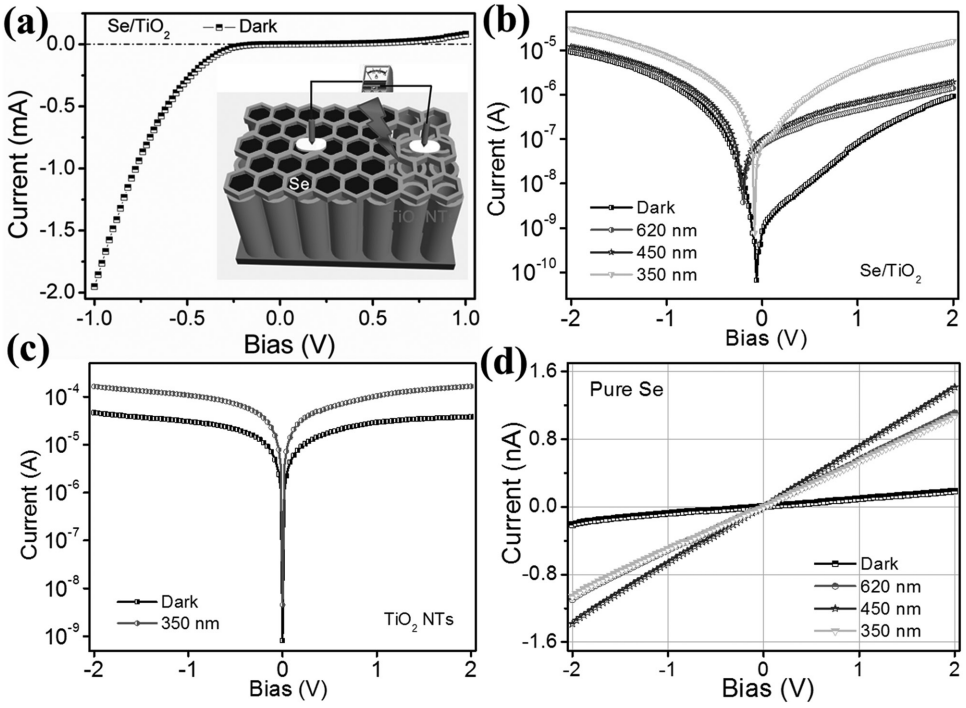

Figure 4. Typical *I–V* curves for Se/TiO_2 photodetector device a) in the dark, and b) under light illumination of 620, 450, and 350 nm. Inset in (a) shows the schematic device illustration. c,d) *I–V* curves for pristine TiO_2 NTs device and pure Se device, respectively.

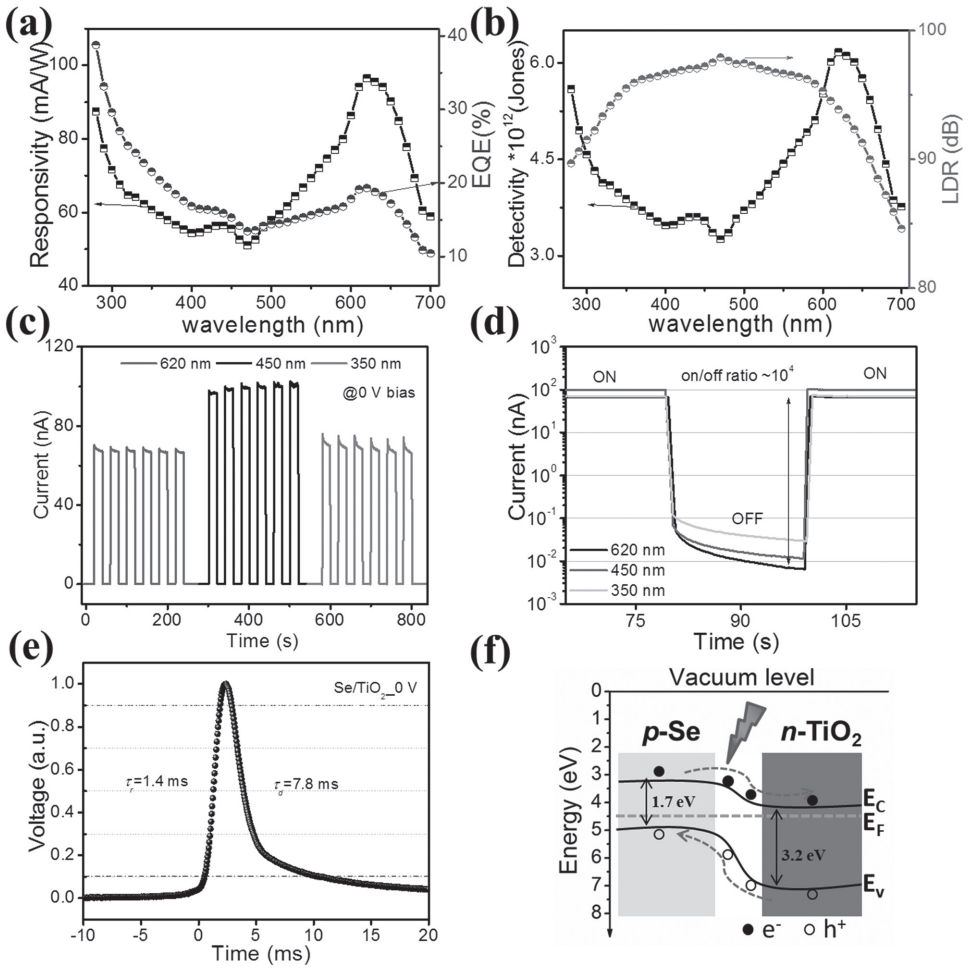

Figure 5. a) Spectral responsivity and EQE spectra b) detectivity and linear dynamic range spectra for Se/TiO_2 device as a function of wavelength at zero bias. c) Time-dependent photocurrent response under chopped light irradiation of 620, 450, and 350 nm at zero bias. d) Enlarged one cycle of semilog *I–t* curves in (c). e) Temporal voltage response, highlighting the rise, and decay times. f) Energy band diagram of Se/TiO_2 type-II heterojunction.

to that of Se/TiO_2 device from which can be deduced that Se plays a significant role in the broadband photoresponse in the photovoltaic mode, consistent with the *I–V* results in Figure 4. It can be explained by the UV–vis diffuse reflectance spectra (DRS) as shown in Figure S3c,d in the Supporting Information. The TiO_2 NTs exhibit intense spectral response only in the UV range with a wavelength below 390 nm (absorption peak at 357 nm), which can be ascribed to the large energy band gap of anatase TiO_2. The weak absorption in the visible light region (400–700 nm) is possibly owing to the light scattering caused by pores/cracks in the nanotubes (Figure S3c, Supporting Information).[37,38] While for pure Se sample, the absorption intensity enhances greatly when the wavelength is shorter than 750 nm, and then reaches a peak value at ≈512 nm. It shows broad band light absorption from UV to visible region (Figure S3d, Supporting Information). According to the Kubelka–Munk equation,[32] the relationships between $(\alpha h\nu)^2$ and the photon energy demonstrate that the energy band gaps of TiO_2 NTs and Se sample are ≈3.15 and 1.62 eV, respectively (insets in Figure S3c,d, Supporting Information).

The detectivity (D^*) and linear dynamic range (LDR, typically quoted in dB) are two important figure-of-merits for a PD and the results are shown in Figure 5b. The D^* reflects the ability to detect weak signals from the noise environment. By assuming the shot noise from the dark current is the major contributor, it can be calculated as[39–41]

$$D^* = \frac{R\lambda}{(2eI_d/S)^{1/2}} \quad (3)$$

Owing to the suppressed dark current and enhanced responsivity, the D^* of the heterostructured device is as high as 6.2×10^{12} Jones at the wavelength of 620 nm. This value is within an order of magnitude of the D^* for commercial Si and InGaAs PDs and exceeds the D^* for Ge PDs.[42] It is noteworthy that the high D^* (over 10^{12} Jones) in a broadband wavelength range in this study is acquired at zero bias and larger than other self-powered PDs listed in Table 1, also in contrast to high external bias reported in previous reports.[43–45] The LDR can be expressed from the equation[39]

$$\mathrm{LDR(dB)} = 20\log(I_{ph}/I_d) \quad (4)$$

The LDR is calculated to be 94 dB at 620 nm, 97 dB at 450 nm, and 96 dB at a wavelength of 350 nm (Figure 5b),

much larger than those of InGaAs PDs (66 dB).[46] The high LDR (over 80 dB in the range of 280–700 nm) indicates a relatively large ratio of photocurrent to dark current and a high signal-to-noise ratio.

Reliability and fast response to light illumination are crucial to high-performance PDs. The temporal photoresponse of the Se/TiO_2 hybrid PD was measured at zero bias under three wavelengths illumination (620, 450, and 350 nm), and the results are shown in Figure 5c,d. The on/off switching is reproducible and stable without notable photocurrent-decay for multiple cycles. Interestingly, the device demonstrates an ultrahigh photosensitivity (defined as $((I_{ph}–I_d)/I_d)$ up to four orders of magnitude without an external bias upon both UV and visible light illumination, as shown in the enlarged graph of one on-off cycle (Figure 5d). The photosensitivities under zero bias are calculated to be 11452, 8413, and 2817 for the wavelengths of 620, 450, and 350 nm, respectively. The maximum photocurrent can reach up to 10^{-7} A at zero bias when illuminated by 450 nm light. The rise time τ_r (peak photocurrent increase from 10% to 90%) and decay time τ_d (peak photocurrent drop from 90% to 10%) of the present Se/TiO_2 device are estimated to be 1.4 and 7.8 ms at zero bias (Figure 5e), respectively. The superior photosensitivity and ultrafast response speed are comparable to the similar type (Table 1) and promise great potential applications in future optoelectronic devices.

The energy band alignment of the type-II Se/TiO_2 heterojunction is elucidated in Figure 5f. A depletion region is developed at the interface between p-type Se and n-type TiO_2 by carrier diffusion under thermal equilibrium conditions, and it gives a built-in electric field which changes the band bending at the interface and provides a driving force for the separation of electrons and holes.[47,48] Upon above-bandgap light illumination, the photogenerated electron–hole pairs could be separated at faster rate by the built-in electric field inside the depletion region. Forced by the electric field, the electrons are directed to the conduction band of the n-type TiO_2 while the holes are moved toward the valence band of the p-type Se, leading to the generation of a photovoltaic current in the external circuit. In addition, the minority carriers generated within the diffusion length from the depletion region could also diffuse to the depletion region and be

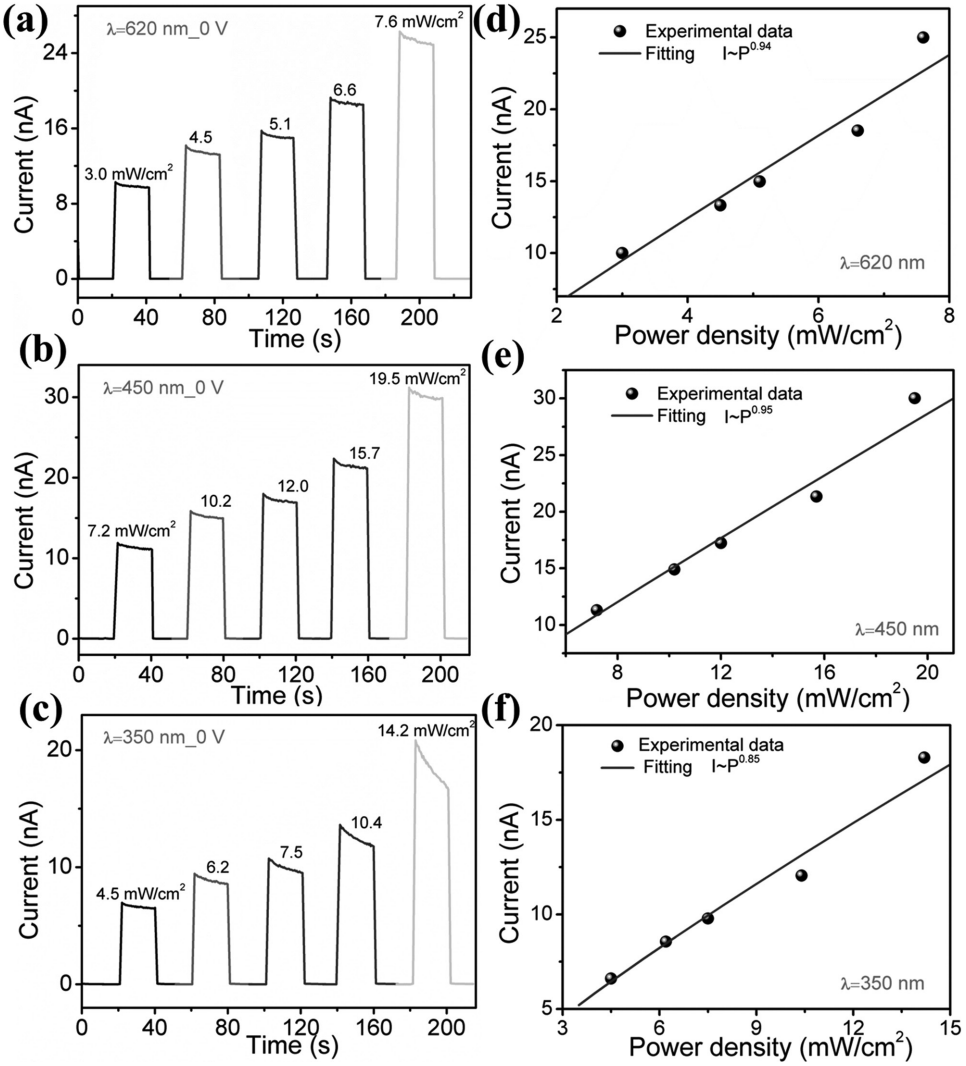

Figure 6. a–c) Time-dependent photocurrent response at zero bias upon 620, 450, and 350 nm light illumination at different light intensities, respectively and d–f) their corresponding fitting curves for the relationship between the photocurrent and the light intensity.

extracted by the built-in electric field. The photovoltage is a result of the energy difference between the Fermi levels of Se and TiO_2 under illumination. This photovoltaic effect enables the present heterojunction device to sense UV–visible light without any external energy supply.

In addition, the photosensitivity of a PD was also examined using a range of irradiances of 3–20 mW cm^{-2} light intensities (**Figure 6**). Steadily increasing photocurrent responses with respect to the increased light intensities are observed for all the three wavelengths as shown in Figure 6a–c, giving photocurrent values of 25.6 nA at 7.6 mW cm^{-2} for 620 nm light, 30.0 nA at 19.5 mW cm^{-2} for 450 nm light, and 18.3 nA at 14.2 mW cm^{-2} for 350 nm light. This observation is consistent with the fact that the charge carrier photogeneration efficiency is proportional to the absorbed photon flux. The nonlinear relationship for the variation of photocurrent against irradiance intensity can be fitted by the power law[49–51]

$$I_{ph} = AP^{\theta} \tag{5}$$

where A is a constant for a certain wavelength, and the exponent ($0.5 < \theta < 1$) determines the response of the photocurrent to light intensity. By fitting the curves in Figure 6d–f with this equation, the values of θ are calculated to be 0.94, 0.95, and 0.85 at wavelengths of 620, 450, and 350 nm, respectively. This fractional power dependence is likely to be related to the complex processes of electron–hole generation, recombination, and trapping within the self-powered device.[26,52–54]

To better understand the physical mechanism of the self-powered broadband Se/TiO_2 device, we further examined the photoresponse under +1 V and –1 V biases at three different wavelengths of 620, 450, and 350 nm. As displayed in **Figure 7**a, the photocurrent increases to 0.65 mA with an on/off ratio of ≈3.6 at +1 V bias under 620 nm light irradiation. The square-wave curves indicate that the device has a fast response speed, and the rise and decay times are estimated to be less than 0.3 s (limitation of the measurement system). This behavior is very similar to that of pure Se device (Figure S4a,b, Supporting Information) as Se functions dominantly in the photodetection for Se/TiO_2 hybrid device. Interestingly, the *I–t* curves under illumination of 450 nm are undergoing two processes (Figure 7b) at +1 V bias. i.e., the photocurrent first increases steeply (quick process) and then slightly to a steady value (slow process) upon light-on. Accordingly, it falls quickly at first and then decays slowly when light is off. The quick process is similar to that under 620 nm light illumination (response time < 0.3 s), while the slow process takes ≈10 s. Similar phenomenon can be observed when using 350 nm light illumination at +1 V as shown in Figure 7c,d. And it takes much longer for the slow processes (τ_r = 67.4/τ_d = 76.7s), even comparable to the response time for pristine TiO_2 NTs device (Figure S4c,d, Supporting Information). When applying a reverse bias of –1 V, only 350 nm UV light can activate the Se/TiO_2 while no obvious photoresponse is detected upon the other two wavelengths light illumination (620 and 450 nm). The reason can be explained by the band alignment as shown in Figure 7e,f. Under forward bias (+1 V, Figure 7e), the width of the depletion layer narrows (the height of the barrier becomes low), hence the photogenerated electron–holes can transport through the depletion layer driven by the applied bias. In contrast, under a reverse bias of –1 V (Figure 7f), the width of the depletion layer appears to be larger, and the generated electrons in the space charge region of TiO_2 cannot pass across the barrier. Thus it is difficult to detect photocurrent response at –1 V under 620 and 450 nm light illumination. While using 350 nm UV light illumination, much more electron–hole pairs are generated in TiO_2 (E_g = 3.15 eV, corresponding to absorption edge of 394 nm), and the resultant built-in electric field becomes stronger, and thus contributing to a higher photocurrent.

The photoresponses under various environments were further verified. The results in **Figure 8** indicate that the photocurrent under light irradiation of 620, 450, and 350 nm (Figure 8a,b) slightly increases with decreasing gas pressure

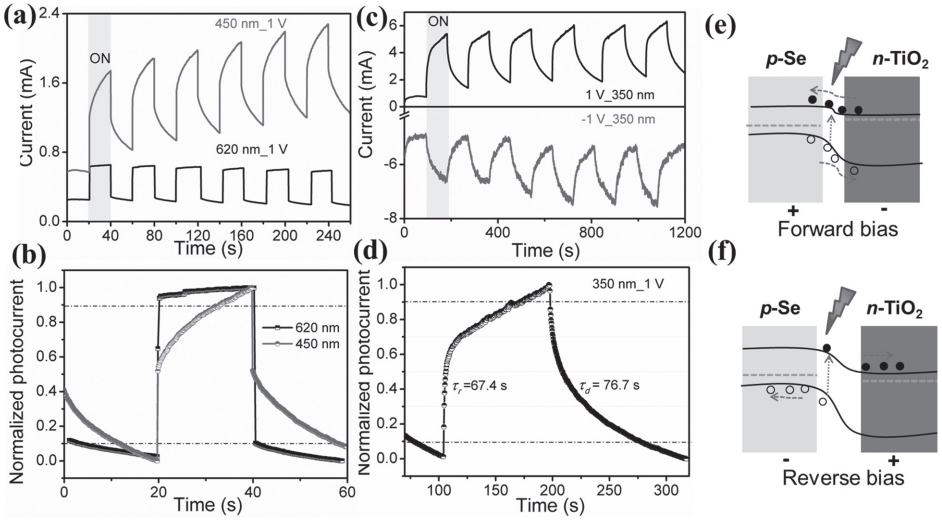

Figure 7. *I–t* curves a) at +1 V bias under light irradiation of 620 and 450 nm and b) their enlarged normalized photocurrent for one cycle. c) *I–t* curves at –1 V and +1 V biases under 350 nm light illumination and (d) the normalized photocurrent at +1 V. e,f) Band alignment at forward bias and reverse bias, respectively.

of the measured environment to 0.2 mPa. Such an observation has been frequently observed in previous studies,[1,50,53] and the reason should be ascribed to the existence of the oxygen chemisorption/desorption on the Se/TiO_2 surface (Figure 8d). Owing to the large surface-to-volume ratio, oxygen molecules are adsorbed onto TiO_2 surface by trapping free electrons from its conduction band, which leads to a low-conductivity depletion region near the surface:[26,55] [O_2 (g) + $e^- \rightarrow O_2^-$ (ad)]. The oxygen adsorption is particularly prominent in the nanotube geometry, where the surface area is large and the depletion layer may extend to a few tens of nanometers which is comparable to the wall thickness of the TiO_2 NTs.[55,56] Upon light illumination, the photogenerated holes move to the surface along the potential gradient produced by band bending and desorb oxygen from the surface resulting in an increase in the free carrier concentration and a decrease in the width of the depletion layer [$h^+ + O_2^-$ (ad) $\rightarrow O_2$ (g)]. This leads to an enhancement of carrier injection, producing a persistent photocurrent. While in vacuum, more oxygen ions can be photodesorbed from the surface of the TiO_2 nanotubes so that the depletion layer is reduced, leading to a higher photocurrent than that in air. The very slow photocurrent decay (≈23 min) upon light switching off as shown in Figure 8c is also attributed to the suppression of oxygen molecules re-adsorption in vacuum.

3. Conclusion

In summary, a novel heterojunction based on Se and 1D self-ordered TiO_2 NTs is facilely prepared and constructed into a high performance photodetector device. The implanting of intrinsic p-type Se broadens the detection range to UV–visible with a large detectivity of 6.2×10^{12} Jones and a high linear dynamic range of 94 dB at 620 nm light illumination. In addition, under zero-bias operation mode, the hybrid device exhibits a good responsivity of ≈100 mA W^{-1}, ultrahigh photosensitivity (on/off ratio up to 10^4), and fast response speed (1.4/7.8 ms). These properties reported here make the Se/TiO_2 broadband photodetectors suitable for large scale device applications that require high response speed, good photosensitivity, and self-sufficient functionality.

4. Experimental Section

Preparation of Anodic TiO_2 NTs: Titanium foils (99.7% purity, 0. 25 mm thick, Sigma Aldrich) were degreased by ultrasonication in acetone, ethanol, and deionized water successively, and then dried in a nitrogen stream before anodization. Anodic TiO_2 NTs were generated in a two-electrode electrochemical cell, with platinum gauze as counter electrode and a Ti foil as working anode. The Ti working anode was pressed together with an Al foil against an O-ring, defining a working area of 1.766 cm^2 (diameter of 1.5 cm). The electrolyte consisted of an anhydrous ethylene glycol solution of 0.27 wt% NH_4F and 5 vol% H_2O. The Ti foils were preanodized in the electrolyte at 70 V for 2 h, and the oxide films were peeled off by employing an adhesive tape. Then they were anodized for a second time in the same but fresh electrolyte at 70 V for 15 min to grow the highly ordered NTs with clean top surface. All the anodization experiments were performed at room temperature. After anodization, the samples were washed with ethanol and then dried in a nitrogen stream. To obtain the anatase TiO_2 NTs, the as-anodized samples were thermally treated at 450 °C in air for 2 h.

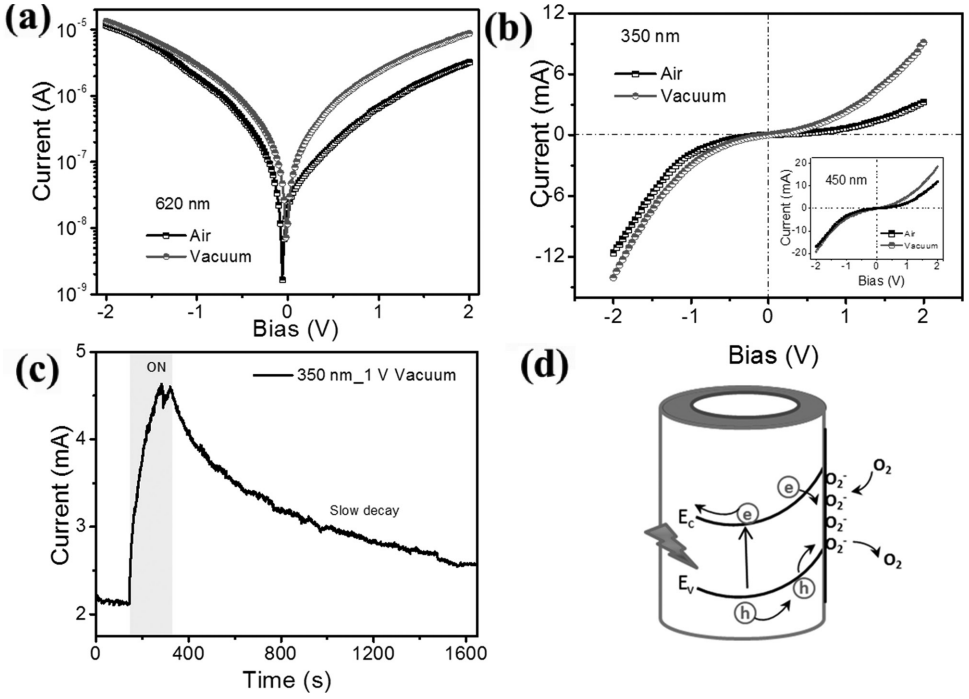

Figure 8. *I–V* curves under air and vacuum (0.2 mPa) conditions under light illumination of a) 620 nm, b) 450 nm, and 350 nm, respectively. c) *I–t* curves under vacuum condition at 1 V bias under 350 nm light illumination. d) Schematic illustration of oxygen adsorption/desorption processes.

Synthesis of Se/TiO_2 Composite: In a typical vapor transport and deposition process, Se source (purity > 99.95%, Meixing chemical co., LTD, Shanghai) was placed in the center of a horizontal tube furnace while half-covered TiO_2 NTs substrate was placed 28 cm downstream from center vertically. Before heating, ultrapure nitrogen was flushed at a rate of 400 sccm for 30 min to remove residual air. Then, the center temperature of tube furnace was heated to 330 °C in 60 min and maintained at 330 °C for 240 min with a constant nitrogen flow of 300 sccm. After that, the furnace was then cooled down to room temperature naturally. For comparison, pure Se samples were synthesized *via* the similar process using a Si wafer with a 200 nm thick SiO_2 top layer as the substrate instead of TiO_2 NTs substrate.

Analysis Instruments: Sample morphologies were characterized using a FE-SEM (Zeiss Sigma). XRD patterns were collected on a Bruker D8-A25 diffractometer using Cu Kα radiation (λ = 1.5405 Å). The XPS spectra were recorded by a Perkin Elmer PHI 5000 C ESCA system equipped with a hemispherical electron energy analyzer, and the Mg-Kα (1253.6 eV) anode was operated at 14 kV and 20 mA. The binding energy for C 1s peak at 284.6 eV was used as the reference for calibration. The optical properties were investigated using a UV–vis spectrophotometer (Hitachi U-3900H) with an integrating sphere attachment.

Photoelectric Measurements: To construct a detector device, small silver pastes with area (≈0.002 cm^2) were doctoral-bladed onto the sample as electrodes. The photoelectric performance was analyzed with an Xe lamp, monochromator, a program-controlled semiconductor characterization system (Keithley 4200, USA). The light intensity was measured with a NOVA II power meter (OPHIR photonics). The response speed of the photodetector was evaluated by a Nd:YAG 355 nm pulsed laser (the laser pulse width was 3–5 ns) and a digital oscilloscope (Tektronix DPO 5140B). All the measurements were performed at room temperature.

Supporting Information

Supporting Information is available from the Wiley Online Library or from the author.

Acknowledgements

The work was supported by the National Natural Science Foundation of China (Grant No. 51471051), Science and Technology Commission of Shanghai Municipality (15520720700), Shanghai Shu Guang Project (12SG01), the Programs for Professor of Special Appointment (Eastern Scholar) at Shanghai Institutions of Higher Learning.

[1] L. F. Hu, J. Yan, M. Y. Liao, H. J. Xiang, X. G. Gong, L. D. Zhang, X. S. Fang, *Adv. Mater.* **2012**, *24*, 2305.
[2] S. Sarkar, D. Basak, *ACS Appl. Mater. Interfaces* **2015**, *7*, 16322.
[3] T. Y. Zhai, L. Li, X. Wang, X. S. Fang, Y. Bando, D. Golberg, *Adv. Funct. Mater.* **2010**, *20*, 4233.
[4] C. Y. Hsu, D. H. Lien, S. Y. Lu, C. Y. Chen, C. F. Kang, Y. L. Chueh, W. K. Hsu, J. H. He, *ACS Nano* **2012**, *6*, 6687.
[5] L. Peng, L. F. Hu, X. S. Fang, *Adv. Mater.* **2013**, *25*, 5321.
[6] Y. Q. Bie, Z. M. Liao, H. Z. Zhang, G. R. Li, Y. Ye, Y. B. Zhou, J. Xu, Z. X. Qin, L. Dai, D. P. Yu, *Adv. Mater.* **2011**, *23*, 649.
[7] J. Qi, X. Hu, Z. Wang, X. Li, W. Liu, Y. Zhang, *Nanoscale* **2014**, *6*, 6025.
[8] M. Zhu, L. Zhang, X. Li, Y. He, X. Li, F. Guo, X. Zang, K. Wang, D. Xie, X. Li, B. Wei, H. Zhu, *J. Mater. Chem. A* **2015**, *3*, 8133.
[9] C. S. Lao, M. C. Park, Q. Kuang, Y. Deng, A. K. Sood, D. L. Polla, Z. L. Wang, *J. Am. Chem. Soc.* **2007**, *129*, 12096.
[10] M. W. Chen, C. Y. Chen, D. H. Lien, Y. Ding, J. H. He, *Opt. Express* **2010**, *18*, 14836.
[11] L. Wang, W. Yang, H. Chong, L. Wang, F. Gao, L. Tian, Z. Yang, *RSC Adv.* **2015**, *5*, 52388.
[12] M. W. Chen, J. R. D. Retamal, C. Y. Chen, J. H. He, *IEEE Electron Device Lett.* **2012**, *33*, 411.
[13] C. Y. Chen, M. W. Chen, C. Y. Hsu, D. H. Lien, M. J. Chen, J. H. He, *IEEE J. Sel. Topics Quantum Electron.* **2012**, *18*, 1807.
[14] B. Tian, X. Zheng, T. J. Kempa, Y. Fang, N. Yu, G. Yu, J. Huang, C. M. Lieber, *Nature* **2007**, *449*, 885.
[15] B. M. Kayes, H. A. Atwater, N. S. Lewis, *J. Appl. Phys.* **2005**, *97*, 114302.
[16] X. S. Fang, Y. Bando, U. K. Gautam, T. Y. Zhai, S. Gradecak, D. Golberg, *J. Mater. Chem.* **2009**, *19*, 5683.
[17] H. Y. Chen, H. Liu, Z. M. Zhang, K. Hu, X. S. Fang, *Adv. Mater.* **2016**, *28*, 403.
[18] H. Elgala, R. Mesleh, H. Haas, *IEEE Commun. Mag.* **2011**, *49*, 56.
[19] V. Gautam, D. Rand, *Adv. Mater.* **2014**, *26*, 1751.
[20] C. Pan, W. Guo, L. Dong, G. Zhu, Z. L. Wang, *Adv. Mater.* **2012**, *24*, 3356.
[21] S. Kim, Y. T. Lim, E. G. Soltesz, A. M. De Grand, J. Lee, A. Nakayama, J. A. Parker, T. Mihaljevic, R. G. Laurence, D. M. Dor, L. H. Cohn, M. G. Bawendi, J. V. Frangioni, *Nat. Biotechnol.* **2004**, *22*, 93.
[22] P. Roy, S. Berger, P. Schmuki, *Angew. Chem. Int. Ed.* **2011**, *50*, 2904.
[23] D. Wang, Y. Liu, C. Wang, F. Zhou, W. Liu, *ACS Nano* **2009**, *3*, 1249.
[24] Z. Liu, M. Misra, *ACS Nano* **2010**, *4*, 2196.
[25] J. R. Jennings, A. Ghicov, L. M. Peter, P. Schmuki, A. B. Walker, *J. Am. Chem. Soc.* **2008**, *130*, 13364.
[26] G. Liu, N. Hoivik, X. Wang, S. Lu, K. Wang, H. Jakobsen, *Electrochim. Acta* **2013**, *93*, 80.
[27] A. El Ruby Mohamed, S. Rohani, *Energy Environ. Sci.* **2011**, *4*, 1065.
[28] L. B. Luo, X. B. Yang, F. X. Liang, J. S. Jie, Q. Li, Z. F. Zhu, C. Y. Wu, Y. Q. Yu, L. Wang, *CrystEngCommun.* **2012**, *14*, 1942.
[29] L. I. Berger, *Semiconductor Materials*, CRC Press, Boca Raton, FL **1997**.
[30] B. Gates, B. Mayers, B. Cattle, Y. Xia, *Adv. Funct. Mater.* **2002**, *12*, 219.
[31] A. Earnshaw, N. Greenwood, *Chemistry of the Elements*, Butterworth-Heinemann, Oxford, UK **1998**.
[32] L. X. Zheng, S. C. Han, H. Liu, P. P. Yu, X. S. Fang, *Small* **2016**, *12*, 1527.
[33] W. Wang, J. Dong, X. Ye, Y. Li, Y. Ma, L. Qi, *Small* **2016**, *12*, 1469.
[34] R. Lei, H. Zhang, P. Tan, Y. Chen, Z. Zhang, Y. Chang, J. Xu, F. Yang, D. Yu, *J. Phys. Chem. B* **2004**, *108*, 4627.
[35] G. Xi, K. Xiong, Q. Zhao, R. Zhang, H. Zhang, Y. Qian, *Cryst. Growth Des.* **2006**, *6*, 577.
[36] S. Y. Zhang, Y. Liu, X. Ma, H. Y. Chen, *J. Phys. Chem. B* **2006**, *110*, 9041.
[37] G. Dai, J. Yu, G. Liu, *J. Phys. Chem. C* **2011**, *115*, 7339.
[38] G. Li, Z. Lian, W. Wang, D. Zhang, H. Li, *Nano Energy* **2016**, *19*, 446.
[39] B. Zhao, F. Wang, H. Y. Chen, Y. P. Wang, M. M. Jiang, X. S. Fang, D. X. Zhao, *Nano Lett.* **2015**, *15*, 3988.

[40] L. Shen, Y. Fang, H. Wei, Y. Yuan, J. Huang, *Adv. Mater.* **2016**, *28*, 2043.
[41] C. Ma, Y. Shi, W. Hu, M.-H. Chiu, Z. Liu, A. Bera, F. Li, H. Wang, L. J. Li, T. Wu, *Adv. Mater.* **2016**, *28*, 3683.
[42] J. R. Manders, T.-H. Lai, Y. An, W. Xu, J. Lee, D. Y. Kim, G. Bosman, F. So, *Adv. Funct. Mater.* **2014**, *24*, 7205.
[43] M. S. Choi, D. Qu, D. Lee, X. Liu, K. Watanabe, T. Taniguchi, W. J. Yoo, *ACS Nano* **2014**, *8*, 9332.
[44] G. Su, V. G. Hadjiev, P. E. Loya, J. Zhang, S. Lei, S. Maharjan, P. Dong, P. M. Ajayan, J. Lou, H. Peng, *Nano Lett.* **2014**, *15*, 506.
[45] C. X. Zhao, Z. M. Liang, M. Z. Su, P. Y. Liu, W. J. Mai, W. G. Xie, *ACS Appl. Mater. Interfaces* **2015**, *7*, 25981.
[46] S. Liu, Z. Wei, Y. Cao, L. Gan, Z. Wang, W. Xu, X. Guo, D. Zhu, *Chem. Sci.* **2011**, *2*, 796.
[47] M. Wang, Y. Hu, J. Han, R. Guo, H. Xiong, Y. Yin, *J. Mater. Chem. A* **2015**, *3*, 20727.
[48] L. Peng, L. F. Hu, X. S. Fang, *Adv. Funct. Mater.* **2014**, *24*, 2591.
[49] D. Wu, Y. Jiang, Y. Zhang, J. Li, Y. Yu, Y. Zhang, Z. Zhu, L. Wang, C. Wu, L. Luo, J. Jie, *J. Mater. Chem.* **2012**, *22*, 6206.
[50] H. Kind, H. Yan, B. Messer, M. Law, P. D. Yang, *Adv. Mater.* **2002**, *14*, 158.
[51] Q. Hong, Y. Cao, J. Xu, H. Lu, J. He, J. L. Sun, *ACS Appl. Mater. Interfaces* **2014**, *6*, 20887.
[52] H. Y. Chen, K. W. Liu, X. Chen, Z. Z. Zhang, M. M. Fan, M. M. Jiang, X. H. Xie, H. F. Zhao, D. Z. Shen, *J. Mater. Chem. C* **2014**, *2*, 9689.
[53] H. Liu, Z. M. Zhang, L. F. Hu, N. Gao, L. W. Sang, M. Y. Liao, R. Z. Ma, F. F. Xu, X. S. Fang, *Adv. Opt. Mater.* **2014**, *2*, 771.
[54] H. Liu, N. Gao, M. Y. Liao, X. S. Fang, *Sci. Rep.* **2015**, *5*, 7716.
[55] Q. Z. J. Zou, K. Huang, N. Marzari, *J. Phys. Chem. C* **2010**, *114*, 10725.
[56] M. Paulose, O. K. Varghese, G. K. Mor, C. A. Grimes, K. G. Ong, *Nanotechnology* **2006**, *17*, 398.
[57] X. Li, J. Wu, N. Mao, J. Zhang, Z. Lei, Z. Liu, H. Xu, *Carbon* **2015**, *92*, 126.
[58] A. A. Hussain, B. Sharma, T. Barman, A. R. Pal, *ACS Appl. Mater. Interfaces* **2016**, *8*, 4258.
[59] L. Wang, J. S. Jie, Z. B. Shao, Q. Zhang, X. H. Zhang, Y. M. Wang, Z. Sun, S.-T. Lee, *Adv. Funct. Mater.* **2015**, *25*, 2910.
[60] Z. Zhang, Q. Liao, Y. Yu, X. Wang, Y. Zhang, *Nano Energy* **2014**, *9*, 237.
[61] D. Xiang, C. Han, Z. Hu, B. Lei, Y. Liu, L. Wang, W. P. Hu, W. Chen, *Small* **2015**, *11*, 4829.

Received: July 22, 2016
Revised: August 16, 2016
Published online: November 17, 2016

